Performance of a silicon monochromator under high heat load

Aleksandr I. Chumakov,[a]*‡ Ilya Sergeev,[b] Jean-Philippe Celse,[a] Rudolf Rüffer,[a] Marc Lesourd,[a] Lin Zhang[a] and Manuel Sánchez del Río[a]

[a]European Synchrotron Radiation Facility, F-38043 Grenoble, France, and [b]Deutsches Elektronen-Synchrotron, D-22607 Hamburg, Germany. *E-mail: chumakov@esrf.fr

The performance of a cryogenically cooled double-crystal silicon monochromator was studied under high-heat-load conditions with total absorbed powers and power densities ranging from 8 to 780 W and from 8 to 240 W mm^{-2}, respectively. When the temperature of the first crystal is maintained close to the temperature of zero thermal expansion of silicon, the monochromator shows nearly ideal performance with a thermal slope error of 0.6 µrad. By tuning the size of the first slit, the regime of the ideal performance can be maintained over a wide range of heat loads, *i.e.* from power densities of 110 W mm^{-2} (at total absorbed power of 510 W) to 240 W mm^{-2} (at total absorbed power of 240 W).

Keywords: X-ray optics; high-heat-load optics; silicon monochromator; cryogenic cooling.

1. Introduction

A high-heat-load monochromator is often the first optical element of a synchrotron radiation beamline. This makes it also the key element, because the performance of the entire beamline relies on the quality of the X-ray beam provided by the monochromator.

In order to maintain the quality of the X-ray beam, the atomic planes of the monochromator crystals should be flat with a sub-µrad accuracy. The necessity for such a high accuracy can be seen from the following. The slope error $\Delta\theta$ of the crystal surface for a monochromator at a distance L from the source increases the virtual source size by $\Delta z = 2\Delta\theta L$. Therefore, for a typical distance $L = 30$ m, a slope error of 1 µrad increases the virtual source by 60 µm. This is larger than the vertical size of the source at most synchrotron radiation facilities and, therefore, should be avoided.

Preserving the ideal shape of the crystal surface with sub-µrad accuracy is not easy in general, and particularly difficult for the high-heat-load monochromator, where the first crystal is exposed to a powerful X-ray beam. For silicon crystals, the problem can be solved by cryogenic cooling (Bilderback *et al.*, 2000): maintaining the crystal temperature near the temperature of zero thermal expansion ($\sim$125 K for silicon) efficiently reduces thermal deformations caused by a temperature gradient on the crystal surface. Recent calculations show that under these conditions the slope error[1] of the crystal can be kept below 1 µrad (Zhang *et al.*, 2013). However, most studies still report large (>5 µrad) thermal

distortions (Lee *et al.*, 2000, 2001; Carpentier *et al.*, 2001; Tajiri *et al.*, 2001; Zhang *et al.*, 2003, 2013), while the ideally expected sub-µrad flatness of the crystal surface is observed only occasionally (Chumakov *et al.*, 2004).

In this work we study the possibility of reliably reaching sub-µrad flatness of the crystal surface under high-heat-load conditions. The results show that the ideal performance of the silicon monochromator can indeed be achieved and, moreover, maintained over a wide range of storage ring currents, total absorbed power and power density.

2. Monochromator design

The study was performed at the Nuclear Resonance beamline ID18 (Rüffer & Chumakov, 1996) at the European Synchrotron Radiation Facility (ESRF). The high-heat-load monochromator[2] is located at 30 m from the source. It consists of two silicon crystals of size 80 mm (length) × 30 mm (width) × 40 mm (height). The monochromator operates in a vertical scattering geometry with symmetric Si (hhh) reflections, most commonly with Si (111), where the energy of the reflected radiation can be tuned from 6 to 78 keV. Both crystals are cooled in series by liquid nitrogen.

Fig. 1 shows the cooling assembly, which is almost identical for the first and the second crystal. The crystal is clamped with 0.5 mm-thick indium foils between two copper heat exchangers (Marot *et al.*, 1992). Temperatures of both crystals are monitored with Pt 100 sensors located in a hole at the butt-end surface of the crystals.

In comparison with the previous report (Chumakov *et al.*, 2004), in this study the pressure of the crystal clamping was

---

‡ Also at National Research Center 'Kurchatov Institute', 123182 Moscow, Russia.
[1] Here and below, all values of the slope error, angular width and beam size are given as full widths at half-maximum (FWHM).

[2] EMG-T9, manufactured by Kohzu Seiki Co. Ltd.
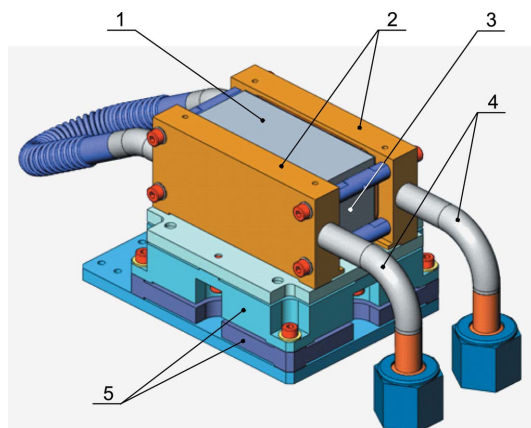
Figure 1
The cooling assembly of the first crystal. 1, silicon crystal; 2, copper heat exchangers; 3, Pt 100 temperature sensor; 4, stainless steel tubes; 5, ceramic thermal isolation plates.

reduced. After being strongly clamped for a few years, the crystals became tightly attached to the copper heat exchangers by the indium foil, and strong clamping was no longer required. Therefore, the torque of the clamping screws was reduced from 15 to ∼3 dN m, which corresponds to a reduction of the clamping pressure from 17 to ∼3 bar. As shown below, relaxing the clamping allows for a smaller static deformation of the crystal but decreases the cooling coefficient.

3. Experimental set-up

The scheme of the experimental set-up is shown in Fig. 2. The beam was provided by three standard ESRF undulators with a magnetic period of 20 mm, magnetic gap of 11 mm and total length of 4.80 m. The beams from the three undulators are aligned to a single axis with an accuracy of 1 μrad. For the storage ring current of 300 mA, the total power of the X-ray beam is 4.1 kW. The front-end diamond window with aperture[3] 2.0 mm × 4.0 mm located at 23.5 m from the source reduces the power of the beam coming to the beamline to ∼1.1 kW. In this study the power load on the monochromator was further limited to ∼0.8 kW by the entrance slit in order to avoid boiling of liquid nitrogen in the closed loop of the cooling system.

The study was performed during a special operation of the storage ring when the electron current was ramped from 10 mA to 300 mA in steps of ∼50 mA. The ramping of the storage ring current is the most direct way to study the effect of the heat load on the monochromator performance, because in this case the distribution of the absorbed power over the crystal surface and along the crystal thickness stays the same. In user operation the storage ring current at the ESRF does not exceed 200 mA. The extended range up to 300 mA was provided exceptionally, in order to test the operation of several beamlines with higher heat load.

---

[3] Here and below, all sizes of the apertures and the beam are referred to as horizontal × vertical.
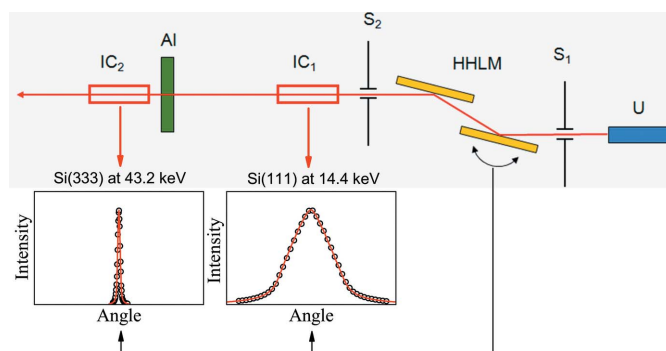
Figure 2
Experimental set-up. U, three undulators; S_1, entrance slit; HHLM, high-heat-load monochromator; S_2, exit slit; IC_1 and IC_2, ionization chambers; Al, 10 mm-thick aluminium absorber. The two graphs show examples of the rocking curves measured by the two ionization chambers.

For each value of the storage ring current the heat load on the monochromator was additionally varied by choosing ten various apertures of the entrance slit S_1. For the smallest apertures, the entrance slit was open to only slightly larger than the beam size (1.2 mm × 0.46 mm) limiting the heat load to the radiation power within the central cone of the utilized X-rays. For the largest apertures the slit was completely open and allowed the monochromator to be exposed to the entire power of radiation after the front-end window (as much as the boiling of liquid nitrogen could be avoided). As shown below, such a combined control of the heat load by the storage ring current and by the aperture of the entrance slit allows for disentangling the influences of the total power and the power density.

For each aperture of the entrance slit the test included measurements of the flux, of the mean slope error of the first crystal, and the slope errors at various positions of the crystal. The mean slope error was evaluated from the width of the rocking curve[4] measured with a large exit slit S_2 (2 mm × 1 mm) accepting the entire beam of the reflected radiation. The slope error at various positions of the crystal was measured with a narrow (2 mm × 0.05 mm) exit slit S_2 accepting the reflected radiation only from the chosen part of the crystal. The vertical offset of the exit slit was varied in the ±0.5 mm range in steps of 0.05 mm. For the given incidence angle $\theta_{in} = 7.9°$, this corresponds to the sampling of the crystal surface in the range ±3.6 mm with a step of 0.36 mm. As discussed below, the measurements of the slope error at various positions of the first crystal allow for deriving the vertical profile of the first crystal surface (Zhang et al., 2013).

In order to study the performance of the monochromator under the nominal operation conditions and to analyze the thermal slope errors with high angular resolution, all tests were performed with two X-rays harmonics. The first ionization chamber IC_1 (Fig. 2) monitored the 14.4 keV radiation emitted by the undulators in the fundamental, which passes

---

[4] Here and below, the term 'rocking curve' denotes the dependence of the radiation intensity at the exit of the monochromator on the angular displacement of the first crystal from the exact Bragg angle. In these measurements the angular position of the second crystal was fixed.

through the monochromator in the Si (111) reflection. These are the most common conditions of the Nuclear Resonance beamline operation, because 14.412 keV is the energy of the nuclear transition for the mostly used ^{57}Fe isotope. However, in this case the large width of the rocking curve (26 µrad) does not allow for precise measurements of the thermal slope errors. The required high angular resolution is achieved by using the second ionization chamber IC$_2$. The 10 mm-thick aluminium filter in front of this chamber absorbs almost entirely the 14.4 keV radiation, but transmits the radiation of higher harmonics. Thus, the second ionization chamber monitors mainly the 42.3 keV radiation emitted by the undulators in the third harmonics, which passes through the monochromator in the Si (333) reflection. In this case, the width of the rocking curve is 1.6 µrad, which allows for the determination of the slope errors with high accuracy.

The 14.4 keV and 42.3 keV radiation components are emitted by the undulators along the same axis and have the same beam size (1.2 mm × 0.46 mm). Therefore, they illuminate the same area of the crystals. The extinction length for the Si (333) reflection of the 42.3 keV radiation (8.4 µm) is larger than that for the Si (111) reflection of the 14.4 keV radiation (1.5 µm). However, both lengths are much smaller than the power absorption length (~40 µm along the normal to the crystal surface; Zhang *et al.*, 2013). Therefore, both radiation components are sensitive mainly to the surface slope error and are less influenced by the deformations of the bulk volume.

For each current of the storage ring and each aperture of the entrance slit S$_1$, the data collection also included monitoring the temperatures of liquid nitrogen at the entrance and exit of the monochromator, the pressure drop in the cooling loop, and the temperatures of both crystals. This allows for calculations of the power density and the total power of the X-ray beam absorbed by the crystals of the monochromator and for the estimation of the cooling coefficient.

4. Vibrations test

Measurements of sub-µrad slope errors induced by heat load require estimations and, if possible, elimination of the crystal deformation caused by clamping and of the angular vibrations of the crystals induced by the cooling system. The test of the angular vibrations was performed in normal operation mode with a storage ring current of 190 mA using the 43.2 keV radiation passing the monochromator in the Si (333) reflection.[5]

Fig. 3(*a*) shows the time dependencies of the current in the ionization chamber IC$_2$ recorded when the crystal was set to the maximum and to the half-maximum positions of the rocking curve. Fig. 3(*b*) shows the power spectral density for the frequency spectra of the ionization chamber current measured for the crystal at the half-maximum position with the cryogenic pump switched on (with a frequency of 42 Hz) and off. Comparison of the spectra reveals that the cryogenic

<hr/>

[5] A preliminary test showed that with the 14.4 keV radiation and the Si (111) reflection the vibrations are hardly detectable.
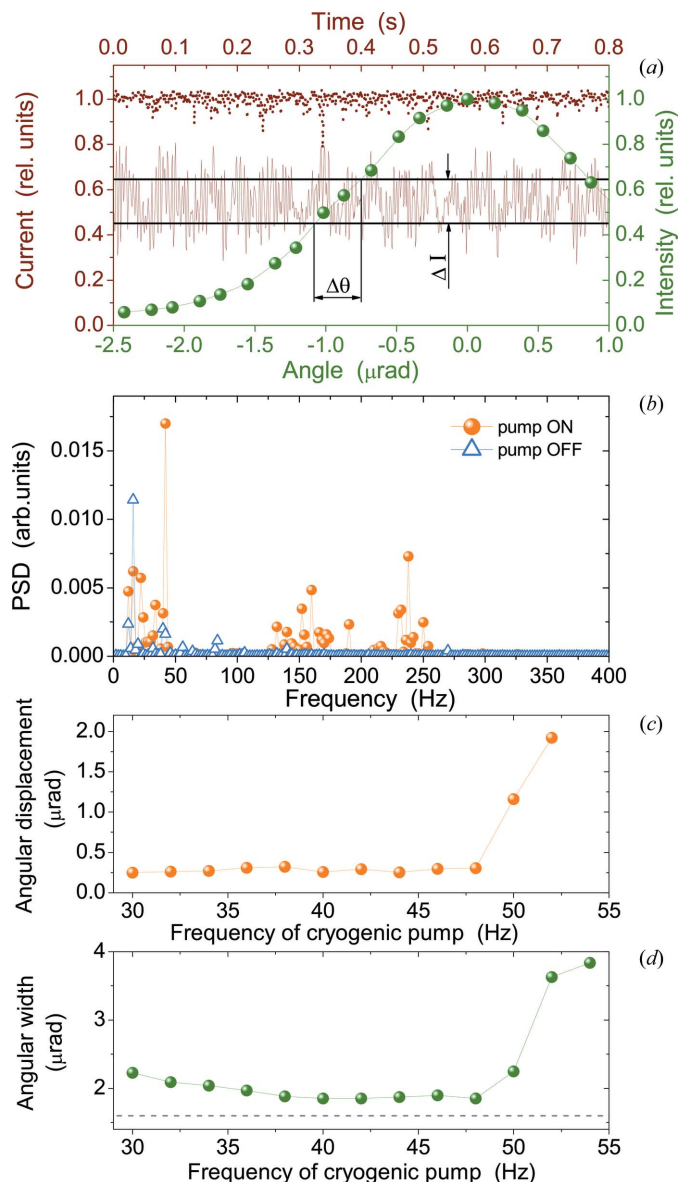
Figure 3
Results of the vibration test. (*a*) Time evolutions of the current in the ionization chamber IC$_2$ at the maximum (dotted line) and half-maximum (solid line) of the rocking curve (left and top axes) superimposed on the plot of the rocking curve (right and bottom axes). The angular displacement of the crystal $\Delta\theta$ is evaluated from the amplitude of the current variation ΔI and the slope of the rocking curve at the half-maximum position. (*b*) The power spectral density (PSD) for the frequency spectra of the current in the ionization chamber IC$_2$ measured at the half-maximum of the rocking curve with the cryogenic pump switched on (with a frequency of 42 Hz) and off. (*c, d*) Dependencies of the derived angular displacement of the crystal $\Delta\theta$ (*c*) and of the rocking curve width (*d*) on the frequency of the cryogenic pump. The horizontal dashed line in (*d*) shows the theoretical width of the rocking curve.

pump induces vibrations with frequencies of 42 Hz and of about 150 and 230 Hz which disappear when the pump is off. The power spectra density components with frequencies below 30 Hz are possibly caused by ground vibrations.

The amplitude of the angular vibrations was determined according to the procedure illustrated in Fig. 3(*a*). It shows two time evolutions of the current in the ionization chamber

IC$_2$ recorded when the crystal was set to the maximum and to the half-maximum positions of the rocking curve. Superimposition of these plots onto the rocking curve shows that the amplitude of the angular vibrations $\Delta\theta$ is obtained by dividing the amplitude ΔI of the variation of the ionization chamber current by the slope of the rocking curve.

Fig. 3(c) shows the derived amplitudes of the angular vibrations for various frequencies of the cryo-pump. Below 48 Hz the amplitude of vibrations is ∼0.25 µrad and does not depend on frequency. Above 48 Hz it increases, revealing excitation of mechanical resonances. The same behavior is observed in the frequency dependence of the rocking curve width (Fig. 3d). In addition, Fig. 3(d) shows a slight increase of the rocking curve width at frequencies below 40 Hz. Because this effect is accompanied by an increasing temperature of the first crystal (not shown) and not observed for the amplitude of vibrations (Fig. 3c), we attribute it to static thermal distortions increasing at weaker cooling.

The choice of the optimal frequency of the cryo-pump is a matter of a compromise between an efficient cooling and avoiding mechanical resonances. For studies discussed below, the frequency of the cryo-pump was set to 45 Hz.
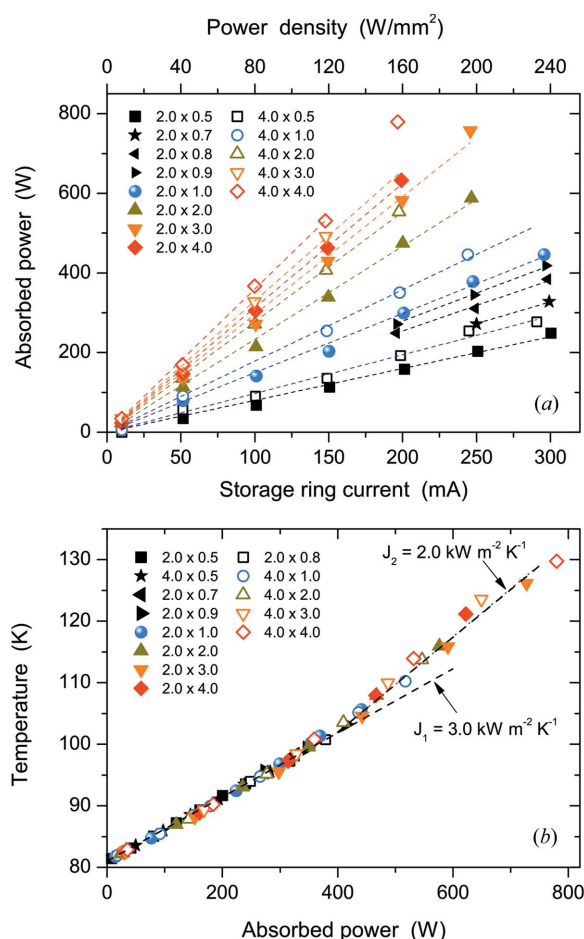
5. Calorimetry

The power of the X-rays absorbed by the monochromator was determined from the difference of the temperatures of liquid nitrogen at the entrance and exit of the monochromator (Chumakov *et al.*, 2004). The results were cross-checked to the temperature differences measured for a calibrated heat load (Rossat, 1999).

Fig. 4(a) shows the absorbed power derived for various currents of the storage ring and various apertures of the entrance slit. The top axis shows the mean absorbed power density.[6] It corresponds to the total absorbed power measured with the 2.0 mm × 0.5 mm entrance slit. According to theoretical calculations using the *SRW* code (Chubar & Elleaume, 1998), the maximal absorbed power density on the axis of the central cone is ∼10% higher than the shown mean absorbed power density.

Fig. 4(a) shows that the total absorbed power increases slower than the area of the entrance slit. This is caused by the non-uniform distribution of the power density over the aperture of the entrance slit and by the shadow effect of the front-end window. The calculated distribution of the beam power at the position of the entrance slit (at 27 m from the source) can be described by the Gaussian horizontal and vertical profiles with FWHMs of 3.4 mm and 2.6 mm, respectively. This distribution is truncated by the upstream front-end aperture of size 2 mm × 4 mm located at 23.5 m from the source. Therefore, the increase of the vertical size of the entrance aperture provides a significant increase of the absorbed power, whereas the increase of the horizontal size from 2 mm to 4 mm increases the absorbed power to a less extent (Fig. 4a).

Figure 4
Results of the calorimetry measurements. (a) Calculated absorbed power for various currents of the storage ring and apertures of the entrance slit. The straight dashed lines show the linear fits to the data obtained with a given slit aperture. (b) The temperature of the first crystal (measured in the middle of the butt-end surface) as a function of the calculated total absorbed power. The dashed lines show the linear fits to the data in two different power ranges allowing for estimations of the cooling coefficients J_1 and J_2.

For each aperture, the data were fit by linear dependencies.[7] These fits are shown by dashed lines. The data points reveal some deviations from the linear fits caused by the limited accuracy of the temperature monitoring. For further analysis we use the data of the linear fits instead of the individual data points. This reduces the uncertainty of the derived absorbed power. For instance, Fig. 4(b) shows the temperature of the first crystal as a function of the absorbed power determined from the linear fits. The data points for all apertures merge to a single 'master curve'. The variance of the derived absorbed power for a constant temperature of the first crystal is only about 20 W. This uncertainty is small and not significant for the further analysis.

All discussion and analysis below are performed in terms of the experimentally determined data of the *absorbed* power and the *absorbed* power density shown in Fig. 4(a). The

---

[6] Note that the variation of the entrance aperture changes the total absorbed power but not the power density.

[7] The data point for the absorbed power of 780 W obtained with the 4 mm × 4 mm entrance slit was excluded from the fit due to an apparent onset of boiling of liquid nitrogen in the closed loop of the cooling system.

comparison of these data with the theoretical calculations using the *SRW* code suggests that the measured absorbed power amounts to about 75% of the expected total power emitted by the undulators. Understanding the origin of the 25% difference between the calculated and the measured power requires further study. The obvious reason could be radiative losses due to Compton, Rayleigh scattering and fluorescence emission. Another source of the losses could be possible errors in the magnetic field of the undulator magnets. In this case the power losses must be related mainly to the high-order harmonics, because the calculated and the measured flux of the 14.4 keV radiation in the fundamental differ only by a few percent.

The dependence of the crystal temperature T on the absorbed power P (Fig. 4b) gives an estimate of the cooling coefficient $J = (dT/dP)^{-1}/S$. Here S is the area of the cooling surfaces [$2 \times (3\ cm \times 8\ cm)$]. Below 400 W, the estimated cooling coefficient is $J_1 = 3.0\ kW\ m^{-2}\ K^{-1}$. The finite-element analysis of the cooling assembly reproduces the experimental data ($T = 95\ K$ at $P = 300\ W$) with the cooling coefficient $J = 3.5\ kW\ m^{-2}\ K^{-1}$, which is close to the estimated value. The smaller value of the estimated cooling coefficient can be expected, because the monitored temperature of the butt-end surface of the crystal is higher than the temperature of the side surface attached to the heat exchanger. Above 400 W the slope dT/dP increases, giving a lower estimated coefficient of $J_2 = 2.0\ kW\ m^{-2}\ K^{-1}$. This is possibly caused by a decrease of the silicon thermal conductivity with temperature, which leads to an additional increase of the temperature difference between the side and the butt-end surfaces of the crystal.

We note that in previous studies (Chumakov *et al.*, 2004) with stronger clamping of the crystals the estimated cooling coefficient was $\sim 9\ kW\ m^{-2}\ K^{-1}$. Thus, relaxing the clamping decreases the cooling coefficient. On the other hand, as shown below, it largely reduces the static deformation of the crystals.

6. Measurements with 14.4 keV radiation

Fig. 5 shows the results of the flux and the rocking curve width measurements with the 14.4 keV radiation plotted as a function of the storage ring current [Figs. 5(*a*)–5(*c*)] and total absorbed power [Figs. 5(*d*)–5(*f*)]. Up to the nominal limit of the storage ring current (200 mA), the heat-load effects are not visible for the entrance apertures comparable with the
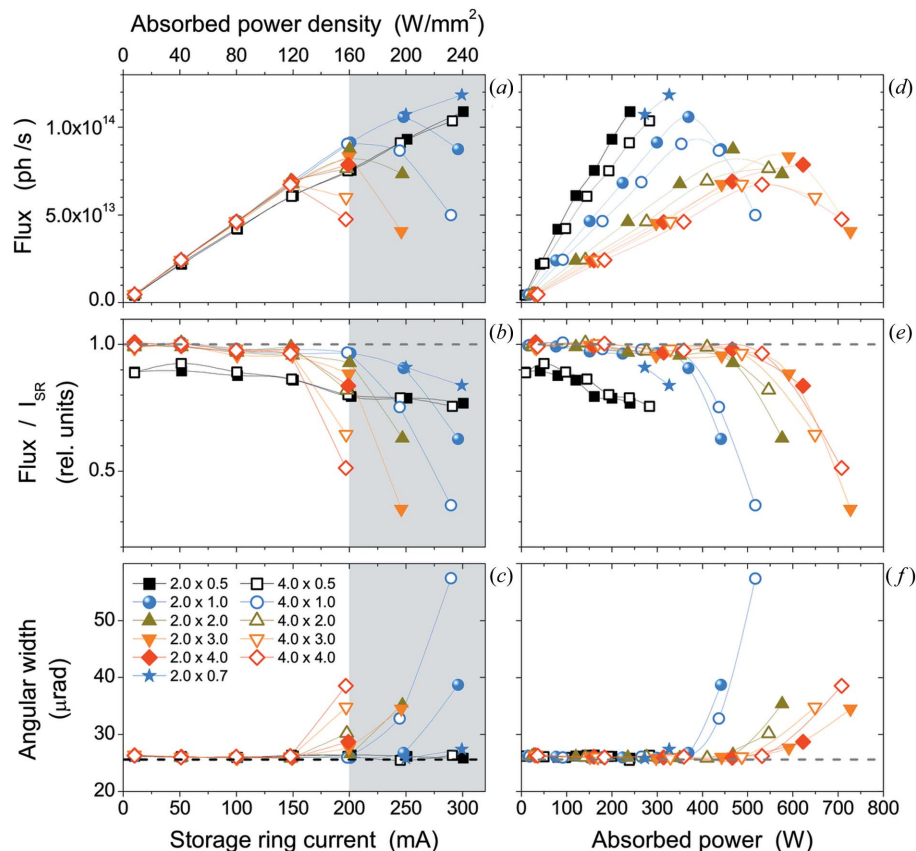
Figure 5
Results of the measurements using the Si (111) reflection of the 14.4 keV radiation. The absolute flux (*a*, *d*), the flux divided by the storage ring current I_{SR} (*b*, *e*), and the rocking curve width (*c*, *f*) for various apertures of the entrance slit are shown as functions of the storage ring current (*a*–*c*) and of the absorbed power (*d*–*f*). The filled areas in (*a*–*c*) mark the region above the nominal operation current of 200 mA. The horizontal dashed lines in (*b*, *e*) indicate the unit level of the flux-to-current ratio; the horizontal dashed lines in (*c*, *f*) show the theoretical width of the rocking curve.

beam size (1.2 mm × 0.46 mm). The flux increases with the storage ring current (Fig. 5*a*), the ratio of the flux to the ring current I_{SR} stays constant[8] (Fig. 5*b*), and the rocking curve does not show any detectable broadening (Fig. 5*c*).

At higher current, the flux still continues to increase for the entrance apertures comparable with the beam size. In particular, at 300 mA the flux reaches the value of 1.2×10^{14} photons s^{-1}. However, the ratio of the flux to the current starts to decrease revealing flux losses. An excessive opening of the entrance slit beyond the central cone leads to severe losses of the flux and broadening of the rocking curve starting from the storage ring current of 200 mA for very large entrance apertures and from 250 mA for smaller ones. In terms of the absorbed power [Figs. 5(*d*)–5(*f*)], these heat-load effects start to become visible at ~ 400 W for small entrance apertures and at ~ 600 W for the larger ones.

Thus, with an opening of the entrance slit slightly larger than the central cone, an acceptable performance of the

---

[8] For the 2.0 mm × 0.5 mm and 4.0 mm × 0.5 mm entrance slits (solid and open black squares, respectively), it is somewhat smaller than for other apertures due to the onset of blocking the central cone by the entrance slit in the vertical direction.

monochromator is observed for storage ring currents up to 300 mA and an absorbed power up to ~400 W.

7. Measurements with 43 keV radiation

7.1. Mean slope error

Fig. 6(a) shows the width of the rocking curve as a function of the storage ring current for four selected apertures of the entrance slit. Fig. 6(b) shows the same data as a function of the absorbed power. The plots reveal the behavior expected from the temperature dependence of the thermal expansion of silicon.

At lowest heat load, the thermal effects are negligible, and the width of the rocking curve is close to the theoretical value. Increasing heat power causes the broadening of the rocking curves. For negative thermal expansion at low temperatures, this is related to the concave ('thermal dent') deformation of the crystal surface. Further increase of the heat load increases the temperature gradient but decreases the modulus of the expansion coefficient. Therefore, the crystal deformation decreases and the rocking curves become narrower. When the crystal temperature comes close to the temperature of zero thermal expansion of silicon,[9] the large temperature gradient is accompanied only by a marginal gradient of the lattice constant. Accordingly, the width of the rocking curves decreases almost to the theoretically expected value. With the further increase of the heat load, the expansion coefficient becomes positive. Under these conditions the temperature gradient leads to the convex ('thermal bump') deformation of the crystal surface. Therefore, the width of the rocking curves again increases. Note that in the previous report (Chumakov et al., 2004) the initial increase of the rocking curve width at negative thermal expansion was not clearly observed due to the large (~4 μrad) convex static deformation of the crystals caused by a stronger clamping.

For the nominal aperture of the entrance slit of 2 mm × 1 mm, the best performance of the monochromator is observed for a storage ring current of ~200 mA and an absorbed power of ~300 W. With the smaller aperture (2 mm × 0.5 mm), the best performance can be reached at almost the same power but much larger storage ring current (~310 mA). An excessive opening of the entrance slit much beyond the beam size shifts the regime of the best operation to a smaller storage ring current (~150 mA). In addition, with a large entrance slit the crystal deformation (broadening of the rocking curve) in the regime of negative thermal expansion becomes smaller.

Owing to the finite step size of the current ramping, the conditions of zero thermal expansion were not exactly met for all apertures of the entrance slit. For instance, for the 2 mm × 0.5 mm and 2 mm × 1 mm slits the solid lines in Fig. 6 indicate

[9] Under the optimal conditions of the most flat crystal surface, the temperature at the center of the beam spot should be apparently somewhat larger than 125 K, so that the onset of the convex deformation of the slightly overheated surface can compensate for the remaining concave deformation of the under-heated deeper volume.
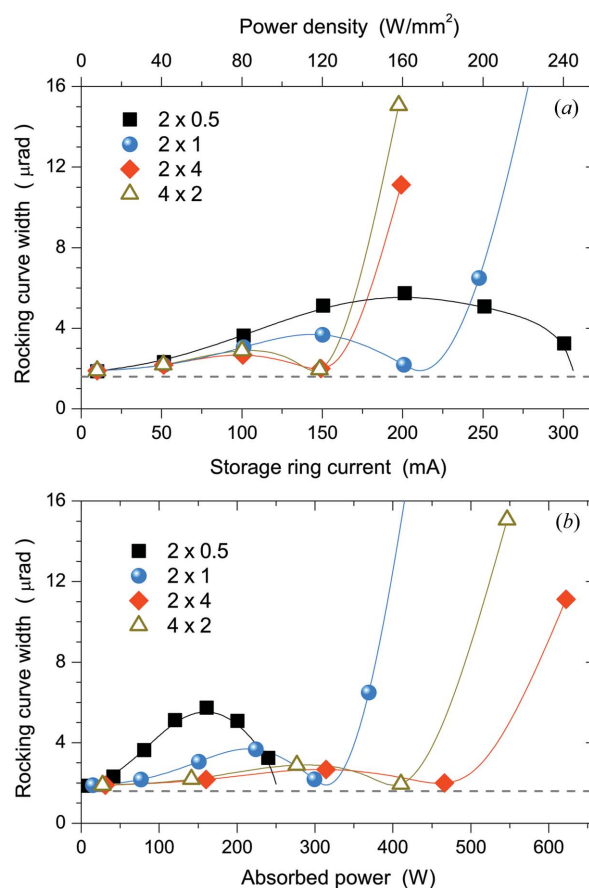
Figure 6
Rocking curve width of the Si (333) reflection of the 43.2 keV radiation for various apertures of the entrance slit shown as a function of the storage ring current (a) and of the absorbed power (b). The solid lines show the spline interpolations of the data sets which, in addition to the experimental data, include the expected position of the ideal performance of the monochromator (see the text). The horizontal dashed lines show the theoretical width of the rocking curve.

the expected (but not spotted in the experiment) positions of the smallest rocking curve widths in terms of the ring current (Fig. 6a) and the absorbed power (Fig. 6b). These positions were estimated by the analysis of the crystal curvatures as explained below.

For the 2 mm × 4 mm and 4 mm × 2 mm slits, the estimated positions of the smallest rocking curve widths coincide with the experimental points almost exactly (Figs. 6a, 6b). This allows for the determination of the thermal slope error under the reached conditions of zero thermal expansion. At smallest heat load, the rocking curve width for the 2 mm × 4 mm and 4 mm × 2 mm apertures is 1.89 (1) μrad. It includes the contribution of the ideal rocking curve width (1.60 μrad), the angular amplitude of crystal vibrations (0.25 μrad) and the static deformation of the crystal. Under a usual assumption of the Gaussian distribution of the slope errors, these contributions add in quadrature. Thus, the static deformation of the crystals is $(1.89^2 - 1.6^2 - 0.25^2)^{1/2}$ μrad = 1.0 (1) μrad. For the condition of zero thermal expansion met in the experiment for the 2 mm × 4 mm and 4 mm × 2 mm slits, the rocking curve width is 1.98 (4) μrad. It includes the additional contribution

of the thermal slope error. Thus, the mean thermal slope error is $(1.98^2 - 1.89^2)^{1/2}$ µrad = 0.6 (1) µrad.

7.2. Profile of the crystal surface

For further analysis we assume that the heat-load effects influence only the first crystal and not the second one. This is plausible because the power of the beam *diffracted* by the first crystal is negligible (<1%); the power of the radiation *scattered* by the first crystal is small (~10%; Zhang *et al.*, 2013) and homogeneously distributed over the surface of the second crystal.

Under these conditions the second crystal acts as the angular reference. If the atomic planes of the first crystal deviate from the nominal position by some angle $\Delta\theta$, the rocking curve of the first crystal will be centered at the angular position $-\Delta\theta$. Thus, the angular shift of the rocking curve gives the slope error of the first crystal. It is easy to see that rocking the second crystal does the same but with the opposite sign of the rocking curve displacement.

Applying this simple logic to practice should be considered with some care, because this approach works properly only if the measurements of the rocking curve do not cause a noticeable vertical displacement of the reflected beam. This condition can be expressed as $2\Omega L_S \ll \delta z$, where Ω is the rocking curve width, L_S is the distance from the monochromator to the exit slit, and δz is the step size of the vertical offset. Under these conditions a rotation of the crystal within the rocking curve can shift the beam vertically only slightly, much less than the step of the vertical offset, whereas the rotation of the crystal beyond the rocking curve does not provide an intense reflection. In the opposite case of $2\Omega L_S \simeq \delta z$, the maximum intensity of the rocking curve will occur not when the atomic planes of the two crystals are parallel but when the angular shift of the first crystal $\Delta\theta$ provides the vertical displacement of the beam equal to the chosen vertical offset Δz, *i.e.* at $\Delta\theta = \Delta z/2L_S$. Then even for the ideally flat crystal the rocking curves will not be centered at the same position but displaced linearly with the vertical offset, providing a misleading impression that the crystal shape is concave with the bending radius $R = 2L_S/\theta_{in}$. In this study ($L_S = 1$ m, $\delta z = 50$ µm), the vertical displacement of the beam during the rocking curve measurements was negligible for the utilized Si (333) reflection of the 43.2 keV radiation ($\Omega = 1.6$ µrad). On the contrary, it would be already noticeable if these measurements were performed with the Si (111) reflection of the 14.4 keV radiation ($\Omega = 26$ µrad).

Fig. 7 shows the results of the surface profile measurements for the 4 mm × 2 mm aperture of the entrance slit. Fig. 7(a) shows the dependence of the rocking curve width on the absorbed power measured with the large (2 mm × 1 mm) exit slit, and Figs. 7(b)–7(e) show the shape of these rocking curves for the four chosen power values. At smallest power (30 W) the rocking curve is close to the theoretical calculations (Fig. 7b). At 280 W the rocking curve becomes broader (Fig. 7c). At 410 W it is again narrow and comparable with

the theoretically expected curve. At 550 W it again becomes broad.

Figs. 7(f)–7(i) show the rocking curves measured for the given powers with the narrow (2 mm × 0.05 mm) vertical slit S_2 at various positions of the vertical offset. The angular displacements are given relative to the centers of the rocking curves measured with a widely open (2 mm × 1 mm) exit slit [Figs. 7(b)–7(e)]. Thus, the displacements of the curves give (with an opposite sign) the angular deviations of the atomic planes of the first crystal from the mean value at various positions of the footprint. This defines the angular profile of the crystal as a function of the coordinate along the crystal surface. The integral of this dependence with a variable inte-
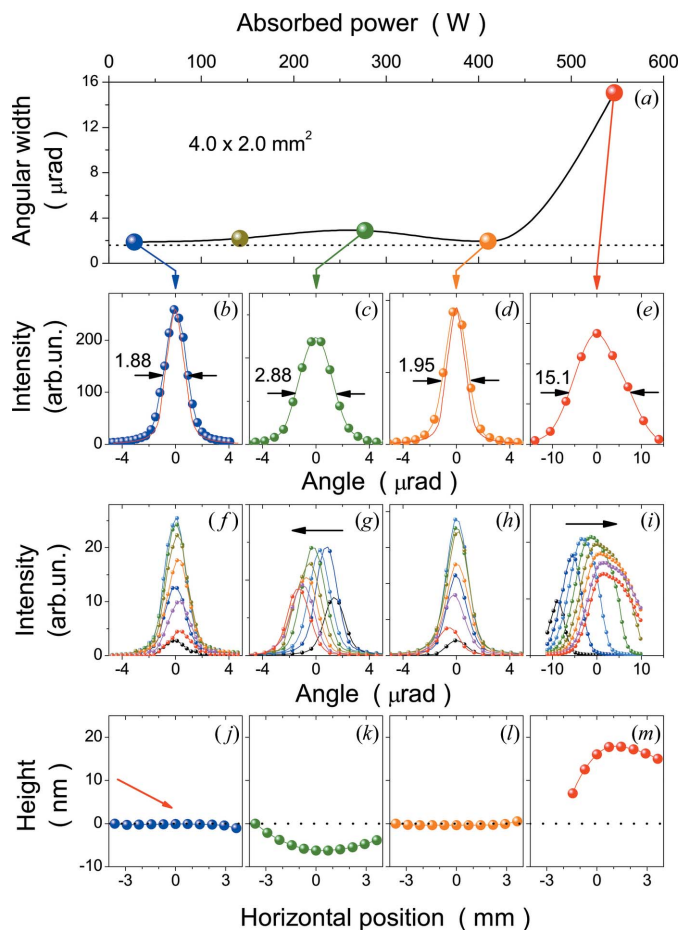
Figure 7
Results of the measurements of the vertical profile of the first crystal performed with the Si (333) reflection of the 43.2 keV radiation and with the 4 mm × 2 mm aperture of the entrance slit. (a) Width of the rocking curve as a function of the absorbed power. The horizontal dashed line shows the theoretical width of the rocking curve. For the four chosen values of the absorbed power marked by the arrows, the lower panels show the rocking curves measured with the fully open exit slit (b–e), with the vertically narrow exit slit positioned at various vertical offsets (f–i) and the derived vertical profile of the crystal surface (j–m). The arrows in (b–e) indicate the FWHM of the rocking curves. The solid lines in (b, d) show the theoretical rocking curves. The arrows in (g) and (i) show the direction of the angular displacements of the rocking curve positions with increasing vertical offset of the exit slit. The horizontal dashed lines in (j–m) show the height of the undisturbed crystal surface. The arrow in (j) schematically shows the direction of the incident X-ray beam.

gration limit gives the vertical profile of the crystal [Figs. 7(*j*)–7(*m*)].

At smallest absorbed power, the rocking curves measured for various vertical offsets are centered at the same position (Fig. 7*f*). Accordingly, the derived profile shows the flat surface (Fig. 7*j*). At higher power (Fig. 7*g*), the rocking curves move to lower angles with increasing vertical offset. This shows that the angle of the atomic planes relative to the incident beam on the downstream part of the crystal surface is larger than that on the upstream part. The derived profile shows the concave shape of the crystal surface (Fig. 7*k*). At 410 W the rocking curves for various offsets are again centered at almost the same position (Fig. 7*h*), revealing that the crystal is again flat (Fig. 7*l*). At higher power (Fig. 7*j*) the rocking curves are again displaced. However, here the displacement is opposite to that at Fig. 7(*g*): the curves move to higher angles with increasing vertical offset. At this heat load the vertical profile reveals the convex shape of the crystal surface.

The combined control of the heat load by the aperture of the entrance slit and by the storage ring current allows one to disentangle the influences of the total power and the power density. Fig. 8(*a*) shows the vertical profiles of the crystal surface for the same power density but different total absorbed powers. With the increase of the total power, the crystal shape varies from concave to almost flat and then to a convex shape. The increase of the power is obviously accompanied by an increase of the mean temperature of the crystal surface at the beam spot position, as shown by the increase of the temperature of the butt-end surface of the crystals indicated in the figure legend. Therefore, Fig. 8(*a*) suggests that the same power density causes the concave shape of the crystal when the mean temperature T of the beam spot is lower than the temperature T_0 of zero thermal expansion of silicon, the almost flat shape when $T \simeq T_0$, and the convex shape when $T > T_0$.

Fig. 8(*b*) compares the vertical profiles for the opposite conditions of the same total power but different power densities. For the same total power and, thus, the same mean temperature of the beam spot, the smaller power density leads to the concave surface, whereas the higher power density causes the convex profile. This shows that the mean temperature of the beam spot is not the only parameter which determines the shape of the crystal surface, and the maximum temperature of the beam spot controlled by the power density also plays a role. For equal mean temperatures, the lower or higher power density can provide the maximum temperature of the beam spot below or above the temperature of zero thermal expansion of silicon, leading to the concave or convex shape of the surface profile, respectively.

The optimal conditions of the ideal performance of the monochromator can be determined from the dependencies of the crystal curvature on the storage ring current. Fig. 9 shows the inverse radius of the crystal curvature for various apertures of the entrance slit. The curvature radius R is calculated from the angular profile of the crystal surface $\theta(x)$ as $R = (\mathrm{d}\theta/\mathrm{d}x)^{-1}$. Here x is the coordinate of the beam spot along the crystal surface.[10] The conditions of the ideal performance of the monochromator are determined by the intersection of the spline interpolation of the data sets with the horizontal line of the infinite radius of the crystal curvature (Fig. 9).

Fig. 9 shows that in terms of the storage ring current the estimated range of the ideal performance of the monochromator spreads from ~150 to ~310 mA. Each value of the optimal storage ring current defines the corresponding values of the total absorbed power P and the power density P/S. Fig. 10 maps the conditions of the ideal performance of the monochromator in the two-dimensional region of these parameters. It spreads from $P = 240$ W and $P/S = 240$ W mm^{-2} to $P = 510$ W and $P/S = 110$ W mm^{-2}. For higher power density the ideal performance occurs at smaller total power. The data sets obtained with the horizontal size of the entrance slit of 2 mm and 4 mm differ from each other. This suggests that, in addition to the power density and total power, the performance of the monochromator depends also on the aspect ratio of the entrance aperture. For instance, at low power densities the optimal performance can be obtained at smaller total power with the larger horizontal aperture.
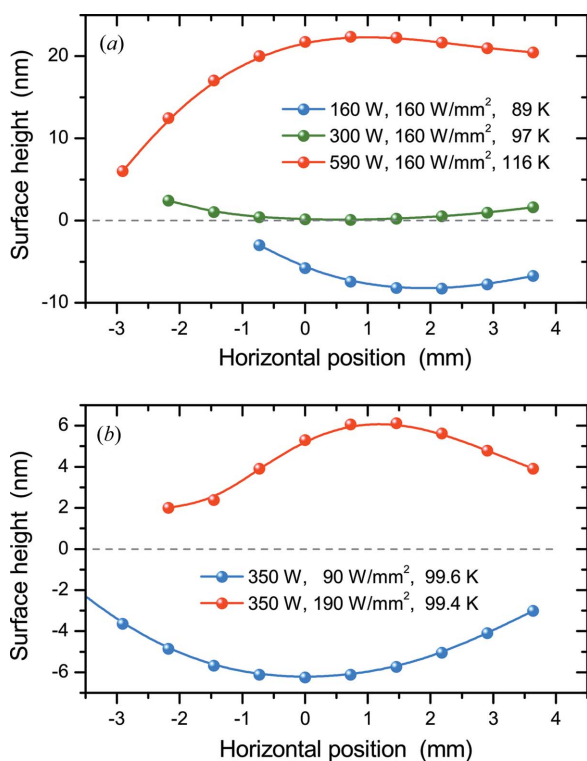
Figure 8
Vertical profile of the crystal surface (*a*) for the same power density but different total absorbed power and (*b*) for the same total absorbed power but different power density. The labels show the values of the total absorbed power, power density and temperature of the butt-end surface of the first crystal. The horizontal dashed lines show the height of the undisturbed crystal surface.

[10] The data show the radius of curvature calculated for the position x_0 of the beam spot which provides the highest intensity of the reflected beam. We note that x_0 coincides with the center of the beam spot only when the crystal is approximately flat. For a significantly curved crystal, both for the concave and convex shape, x_0 is shifted to the downstream side of the beam spot.
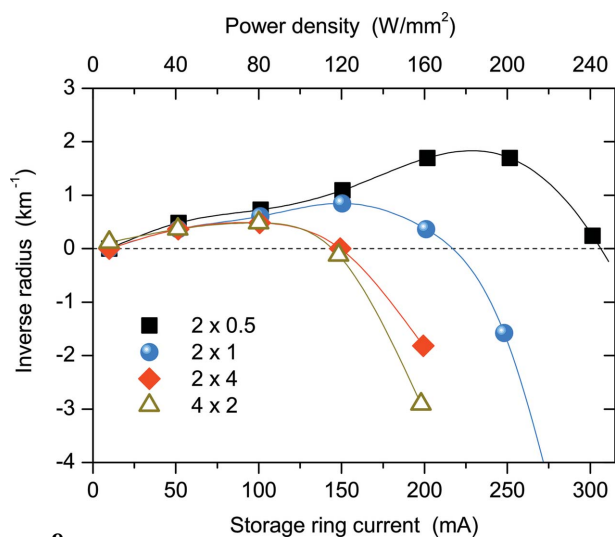
Figure 9
Dependence of the inverse radius of the first crystal curvature on the storage ring current for various apertures of the entrance slit. The positive values correspond to the concave shape of the surface ('thermal dent'), the negative values to the convex shape ('thermal bump'). The solid lines show the spline interpolations of the experimental data points. The horizontal dashed line shows the infinite radius of curvature.

8. Discussion

The obtained results show that the ideal performance of the high-heat-load monochromator can be obtained for a storage ring current in the range 150–310 mA. In particular, it is achieved for the nominal ESRF storage ring current of 200 mA and can be preserved for a possible upgrade of the ESRF operation with a current of 300 mA.

In terms of the absorbed power, the ideal performance of the monochromator is maintained with the power of the central cone[11] varying from 110 to 240 W. This requires a *decrease* of the total absorbed power from 500 to 240 W, which is achieved by closing the entrance aperture from a large opening to the size of the central cone. The yet larger aperture cannot increase the total absorbed power, because it is limited by the size of the front-end window. This determines the *lower* limit of the central cone power at 110 W. Further closing of the entrance aperture could decrease the total power, but would lead to a flux loss. This determines the *upper* limit of the central cone power at 240 W.

The extension of the ideal performance to more intense beams can be achieved with larger cooling coefficients. Fig. 5 of Zhang *et al.* (2003) shows that the increase of the cooling coefficient from 3 to 8 kW m^{-2} K^{-1} shifts the regime of the ideal performance to a $\sim$30% higher power of the central cone, that is, up to $\sim$310 W. As discussed above, the cooling coefficient of 8 kW m^{-2} K^{-1} can be obtained with a stronger clamping of the crystal between the heat exchangers. The increased static deformations of the crystal can be possibly reduced with a more elaborate design of the cooling assembly.

Reaching yet higher central cone powers by further improvements of the crystal cooling seems to be unlikely,

---

[11] For simplicity we define the size of the central cone as 1.67 mm × 0.60 mm = 1 mm^2. Then the central cone power is equal to the power density.
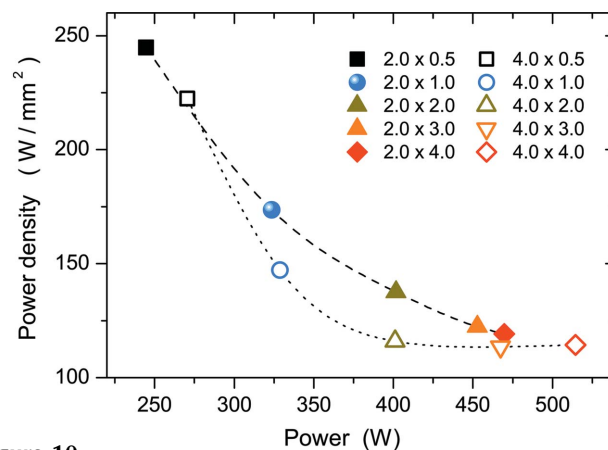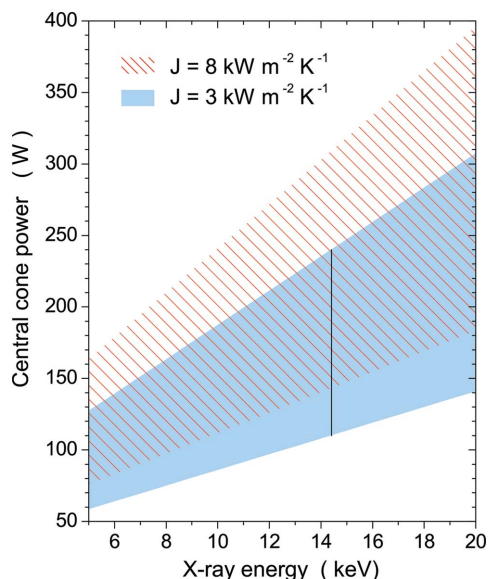

Figure 10
Combinations of the absorbed power density and the total absorbed power required for the ideal performance of the monochromator for various apertures of the entrance slit. The dashed and dotted lines show the spline interpolations of the data sets obtained with the 2 mm- and 4 mm-wide slit, respectively.

because even the increase of the cooling coefficient right up to the theoretical maximum (for side-cooling scheme) of 18 kW m^{-2} K^{-1} (Chumakov *et al.*, 2004) would allow for only a marginal ($\sim$10%) increase of the central cone power (Zhang *et al.*, 2003). Therefore, achieving an ideal performance of the monochromator with the central cone power significantly higher than $\sim$310 W with the discussed design seems to be impossible and would require using either asymmetrically cut silicon crystals or diamond crystals.

The above estimations are valid for the experimental conditions of this study, *i.e.* for the Si (111) reflection of the 14.4 keV X-rays at an incidence angle of 7.9°. Recent calculations (Zhang *et al.*, 2013) show that ideal performance with sub-μrad slope errors can be achieved for a wide range of incidence angles and X-ray energies. However, for softer X-rays and, correspondingly, larger incidence angles it occurs at smaller central cone powers. The analysis of Fig. 11 of Zhang *et al.* (2013) shows that the decrease of the X-ray energy by 1 keV within the 5–17 keV energy range shifts the regime of the ideal performance to a $\sim$12 W lower power of the central cone. This defines the *upper* limit of the central cone power for the X-rays with various energies. The dependence of the *lower* limit of the central cone power on the X-ray energy and on the cooling coefficient is not clear. Assuming that the dependence of the ideal performance on the central cone power varies with the energy of the X-rays and with the cooling coefficient similarly for small and large apertures of the entrance slit, the heat load range for the ideal performance of the Si (111) monochromator can be estimated as shown in Fig. 11. However, the details of the monochromator performance in the limit of the low central cone power and large total absorbed power require further investigations.

The application of the results of this work to other synchrotron radiation facilities may require additional analysis. As mentioned above, the range of the ideal performance depends on the shape and size of the incident radiation beam. Therefore, the obtained results may not be directly

Figure 11
Estimated heat load range of the ideal performance of the Si (111) monochromator for various X-ray energies and for two values of the cooling coefficient *J*. The vertical straight line shows the heat load range of the ideal performance determined for X-rays of energy 14.4 keV.

applicable for facilities with a significantly different size and aspect ratio of the beam.

Furthermore, the range of the ideal performance may depend on the size and shape of the crystals. If the entrance surface of the crystal is essentially larger than the beam spot, this dependence can possibly be reduced to the effect of the cooling coefficient discussed above. If the crystal surface is comparable with the size of the beam spot, the shape of the temperature profile may strongly depend on the crystal shape and bring additional effects.

Finally, we recall that the present analysis is performed in terms of the *absorbed* power and the *absorbed* power density. As mentioned above, the absorbed power is expected to amount to approximately 75% of the total power of the incident radiation. Thus, in terms of the *incident* power density, the heat load range for the ideal performance of the Si (111) monochromator should be about 30% higher than discussed here.

9. Summary

The obtained results show that adjusting the temperature of the crystal surface close to the temperature of zero thermal expansion of silicon allows one to achieve slope errors of thermal deformations as small as 0.6 μrad. By tuning the size of the entrance slit, this performance can be maintained for X-ray beams with a central cone power from 110 to 240 W. At lowest power density, this requires a large opening of the entrance slit providing a total absorbed power of ∼500 W. At highest power density, the entrance slit should be limited by the size of the central cone with a total absorbed power of about 240 W.

References

Bilderback, D. H., Freund, A. K., Knapp, G. S. & Mills, D. M. (2000). *J. Synchrotron Rad.* **7**, 53–60.

Carpentier, P., Rossat, M., Charrault, P., Joly, J., Pirrocchi, M., Ferrer, J.-L., Kaïkati, O. & Roth, M. (2001). *Nucl. Instrum. Methods Phys. Res. A*, **456**, 163–176.

Chubar, O. & Elleaume, P. (1998). *Proceedings of the Sixth European Particle Accelerator Conference (EPAC98)*, pp. 1177–1179. Bristol: Institute of Physics.

Chumakov, A., Rüffer, R., Leupold, O., Celse, J.-P., Martel, K., Rossat, M. & Lee, W.-K. (2004). *J. Synchrotron Rad.* **11**, 132–141.

Lee, W.-K., Fernandez, P. & Mills, D. M. (2000). *J. Synchrotron Rad.* **7**, 12–17.

Lee, W.-K., Fezzaa, K., Fernandez, P., Tajiri, G. & Mills, D. M. (2001). *J. Synchrotron Rad.* **8**, 22–25.

Marot, G., Rossat, M., Freund, A., Joksch, S., Kawata, H., Zhang, L., Ziegler, E., Berman, L., Chapman, D., Hastings, J. B. & Iarocci, M. (1992). *Rev. Sci. Instrum.* **63**, 477–480.

Rossat, M. (1999). Unpublished. (Available by request from AIC.)

Rüffer, R. & Chumakov, A. I. (1996). *Hyperfine Interact.* **97–98**, 589–604.

Tajiri, G., Lee, W.-K., Fernandez, P., Mills, D. M., Assoufid, L. & Amirouche, F. (2001). *J. Synchrotron Rad.* **8**, 1140–1148.

Zhang, L., Lee, W.-K., Wulff, M. & Eybert, L. (2003). *J. Synchrotron Rad.* **10**, 313–319.

Zhang, L., Sánchez del Río, M., Monaco, G., Detlefs, C., Roth, T., Chumakov, A. I. & Glatzel, P. (2013). *J. Synchrotron Rad.* **20**, 567–580.